Published by IOP Publishing for Sissa Medialab

Received: *March 31, 2022*
Revised: *September 19, 2022*
Accepted: *September 28, 2022*
Published: *October 11, 2022*

TECHNICAL REPORT

Design study of an antiproton trap for the GBAR experiment

Kyoung-Hun Yoo,[a] Seok-Ho Moon,[a] Moses Chung,[a,*] Dong Hwan Won,[b] Kwan Hyung Park,[b] Byungchan Lee,[b] Sun Kee Kim,[b,*] Eunhoon Lim,[c] Eun-San Kim,[c] Bong Ho Kim,[d] Dirk van der Werf,[e] Naofumi Kuroda[f] and Patrice Pérez[g]

[a] *Department of Physics, Ulsan National Institute of Science and Theology, Ulsan 44919, Korea*
[b] *Department of Physics and Astronomy, Seoul National University, Seoul 08826, Korea*
[c] *Department of Accelerator Science, Korea University Sejong Campus, Sejong 30019, Korea*
[d] *Center for Underground Physics, Institute for Basic Science, Daejeon 34047, Korea*
[e] *Physics Department, Swansea University, Swansea SA2 8PP, U.K.*
[f] *Graduate School of Arts and Sciences, University of Tokyo, Tokyo 153-8902, Japan*
[g] *Institut de Recherches sur les lois Fondamentales de l'Univers, CEA Saclay, F-91191 Gif-sur-Yvette, France*

E-mail: mchung@unist.ac.kr, skkim@snu.ac.kr

Abstract: The GBAR (Gravitational Behaviour of Antihydrogen at Rest) experiment at CERN has been proposed to measure the gravitational acceleration of the ultracold antihydrogen atoms. This experiment produces antihydrogen ions through interactions between antiprotons and positronium atoms. Then, antihydrogen atoms are produced for the free-fall experiment after the photo-detachment of an excess positron from the cold antihydrogen ions. The energy of the antiproton beam before the positronium target chamber will be in the range of 1–10 keV. The cross-section for the reaction between the antiprotons and positroniums depends mainly on the energy of the antiprotons. Hence, to maximize the productivity of antihydrogen ions, a sufficient number of antiprotons should be provided with well-controlled energy. In this regard, an antiproton trap is considered to accumulate and slow down antiproton beams, and cool them utilizing the electron cooling technique. This trap is designed based on the Penning-Malmberg trap, which consists of a superconducting solenoid magnet

*Corresponding author.

https://doi.org/10.1088/1748-0221/17/10/T10003

2022 JINST 17 T10003

and a series of ring electrodes including high-voltage electrodes to trap antiprotons. In addition, a set of extraction electrodes and optics for beam transport are used. Each electrode has been designed and optimized using the WARP PIC simulations. In this study, the design and simulation results of each trap component are presented.

KEYWORDS: Accelerator Applications; Accelerator modelling and simulations (multi-particle dynamics, single-particle dynamics); Beam dynamics; Instrumentation for particle accelerators and storage rings - low energy (linear accelerators, cyclotrons, electrostatic accelerators)

2022 JINST 17 T10003

Contents

2022 JINST 17 T10003

1 Introduction

The GBAR (Gravitational Behaviour of Antihydrogen at Rest) experiment at CERN aims to measure the free-fall gravitational acceleration of antihydrogen atoms ($\bar{H}$) [1, 2]. The GBAR first combines the antiprotons ($\bar{p}$) with two positrons (e^+), forming antihydrogen ions ($\bar{H}^+$) with a positive charge. Using sympathetic cooling techniques, these ions will be cooled to temperatures of approximately 60 µK before excess positrons are removed through photo-detachment processes [3]. The resultant antihydrogen atoms will be able to fall freely for 20 cm before impact and subsequent annihilation on the chamber floor, whereby the acceleration can be deduced from time-of-flight.

One of the challenges in this experiment is to obtain enough antiprotons with the right phase-space parameters (e.g., energy, temperature, transverse beam size, longitudinal length, etc.) so that antihydrogen ions can be efficiently produced via the following charge exchange reactions in two steps:

$$\bar{p} + Ps \rightarrow \bar{H} + e^-, \; \bar{H} + Ps \rightarrow \bar{H}^+ + e^-. \tag{1.1}$$

Here, the positronium (Ps) target has dimensions of 2 mm × 2 mm cross section and 2 cm length [4]. The energy of the antiproton beam before the positronium target chamber will be in the range of 1–10 keV [5]. Initially, the Antiproton Decelerator (AD) produces 5 MeV antiprotons. These antiprotons are further decelerated to 100 keV by a new deceleration ring called ELENA, then transported to the GBAR beam line. Using a scheme based on electrostatic deceleration in a drift tube, the 100 keV ELENA beam is slowed down to 1 –10 keV [6] before the antiproton trap. Otherwise, energy degrader foils must be used, resulting in a significant loss of antiprotons.

An antiproton trap after the decelerator or degrader can further improve the production efficiency of antihydrogen ions by adjusting the phase-space parameters and accumulating several pulses from

the ELENA. Once a sufficient number of antiprotons, which is targeted $\sim 10^7$, are prepared, they are extracted and transported to the positronium target.

This study developed the GBAR antiproton trap concept and determined its design parameters based on the Particle-In-Cell (PIC) simulations and analytical calculations. Also, the development status of each component of the trap is presented.

2 Design

The main part of the antiproton trap was designed based on the Penning-Malmberg trap configuration with a superconducting solenoid magnet (SC Magnet) and a series of ring electrodes in the trap region [7]. Additional parts include the extractor electrodes and optics for beam transport (figure 1). The design of each part was based on the following concepts.

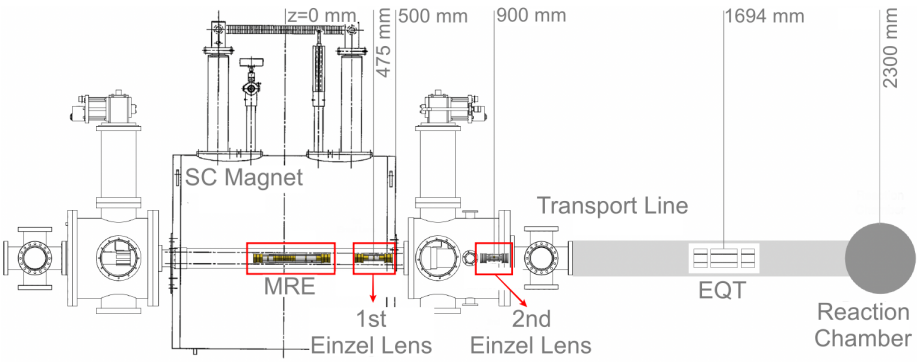

Figure 1. Overall layout of the antiproton trap and beam transport line.

- In the trap region, injected antiprotons are captured in the potential well generated by trap electrodes, and cooled down by the pre-loaded electrons [8].
- The central region of the trap is equipped with a stack of many short ring electrodes [7, 9, 10]. This multi-ring electrode configuration compensates for the distortion of the potential well by the image charges, and generates a near-harmonic potential [11].
- Additionally, to compress antiprotons radially, one of the trap electrodes called rotating wall is segmented by four pieces and generates rotating electric fields while applying the RF voltages with different phases to each segment [12].
- The trap is entirely housed in an ultra-high vacuum (UHV) bore. The UHV bore is maintained at approximately 10–20 K using two GM cryocoolers [7], which allows to satisfy the tight vacuum condition ($\sim 10^{-12}$ mbar) to avoid antiproton annihilation.
- When extracting antiprotons, one einzel lens is used to prevent the beam from diverging by the magnetic field at the exit of the solenoid. Another einzel lens is used to deliver the antiproton beam stably through the transport line. Considering the reaction with positroniums at the reaction chamber, the properties of the antiprotons extracted from the trap must match those of the positroniums. In particular, the beam radius should be as similar as possible. Hence, an electrostatic quadrupole triplet is placed before the reaction chamber.

2022 JINST 17 T10003

2.1 Electrodes in the trap region

Multi-Ring Electrodes (MREs) in the trap region have two high-voltage (HV) electrodes, eleven electrodes including one rotating wall electrode set, and one ground electrode, as shown in figure 2.

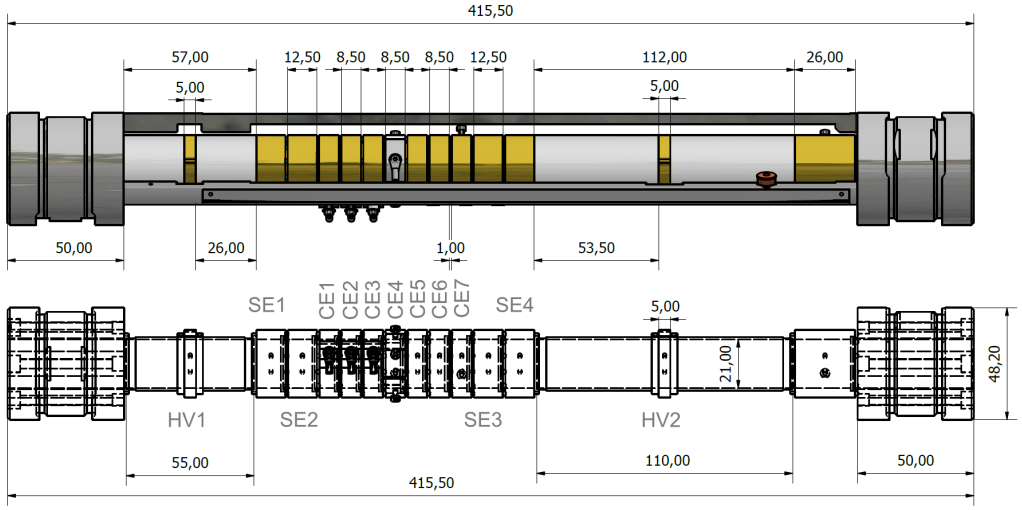

(a)

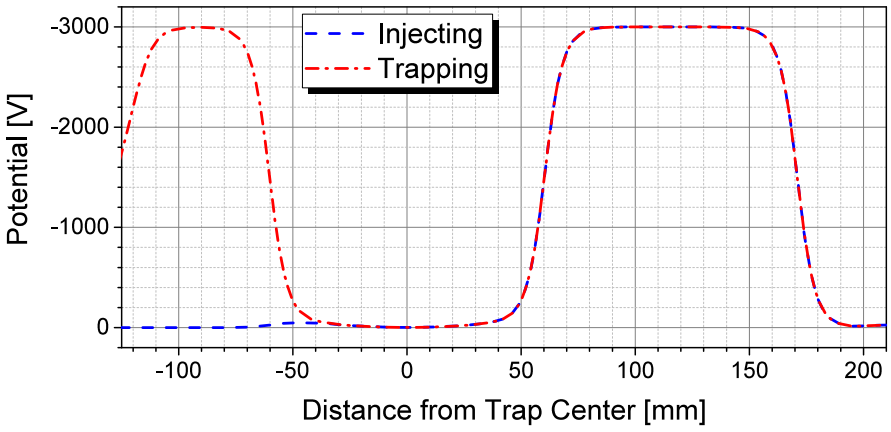

(b)

Figure 2. (a) Design of trap electrodes and (b) on-axis potential distribution for injection and trapping. The trap length was determined in such a way that the round trip distance between HV1 and HV2 is long enough for a ~ 300 ns pulse at 1 keV.

The upstream HV electrode (HV1) is the gate to trap the injected antiprotons, and the downstream electrode (HV2) reflects them. The HV2 was designed longer than the HV1 because the HV2 is used not only for generating the axial potential barrier, but also for accelerating and bunching the antiprotons during the extraction (see section 3.4). We note that the antiprotons are delivered as a short pulse. The eleven electrodes in the central region form the harmonic potential well to trap cooled antiprotons. After cooling, the pre-loaded electrons are removed before further manipulation

2022 JINST 17 T10003

by opening the HV1, SE1-2 and CE1-3. When only antiprotons remain in the trap, their voltages are changed back to original values. The center electrode (CE4) was azimuthally segmented into four pieces to apply the rotating electric field used in the radial compression. It is desirable to couple the rotating electric field to a specific plasma mode in a certain radial compression scenario. In this case, rotating wall electrodes are often placed at the end of the plasma column [12]. This electrode set was installed in a magnetic field of up to 7 T, and the field map is shown in figure 3, matching the center of the trap region to that of the magnet.

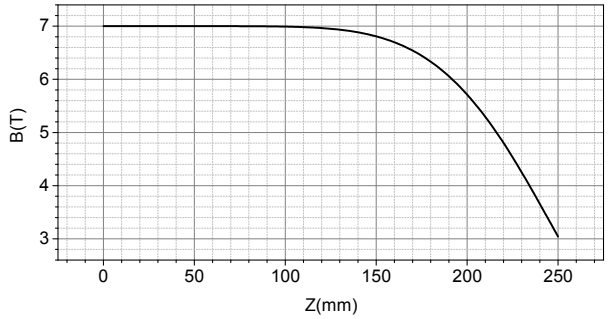

Figure 3. Field map of SC magnet; $z = 0$ means the center of magnet located in the uniform region of the magnetic field where field uniformity is around 0.1%.

2.2 Extraction and transport line

The extracted beam diverges as it exits the high magnetic field and passes the transport line owing to the space-charge effect. Two einzel lenses (figure 4) are used to focus the extracted antiprotons at the end of the magnet and the beginning of the transport line. Both of them consist of two grounded electrodes at both ends and one high-voltage electrode at the center. The position of the first einzel lens is determined based on the magnetic field configuration. The magnetic field lines are diverged after 200 mm from the magnet center (figure 3), thus the extracted antiprotons are also diverged through this region. So, in order to guide the beam without hitting the inner surface of the electrode, we put the first lens at 475 mm, almost at the end of the magnetic field. After the beam simulation with the first lens, we found an additional diverging point of the beam and decided to put the second lens at 900 mm.

For more efficient antihydrogen ion production, the size of the extracted beam should be smaller than that of the positronium target. An electrostatic quadrupole triplet (EQT) (figure 5) reduces the final beam size on the target.

3 Analytical calculation and simulation results

The simulation sequence from the GBAR antiproton trap to the reaction chamber was set as follows:

- Injection and Trapping:
  The injection of antiprotons from the decelerator beam line to the SC magnet and trapping in the multi-ring electrodes was simulated using the WARP Particle-In-Cell (PIC) code [13, 14].

2022 JINST 17 T10003

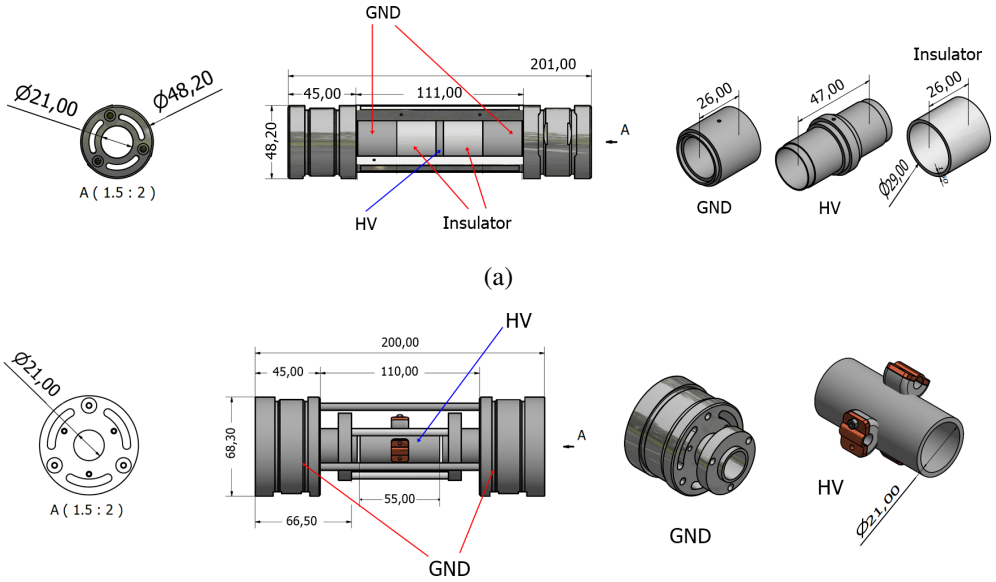

Figure 4. Design of the (a) first and (b) second einzel lenses consisting of two ground electrodes and one high-voltage electrode. In order to avoid interferences with vacuum and cryogenic components, we designed the two lenses differently.

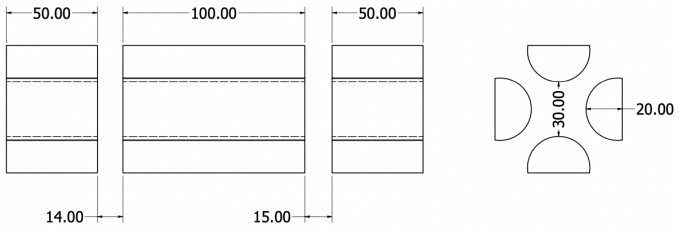

Figure 5. Design of electrostatic quadrupole triplet. The nominal applied voltages are ±170 V.

- Electron Cooling and Radial Compression:
  The cooling time of antiprotons by electrons was calculated from a simplified model (see section 3.2 for more details), and their radially compressed size was estimated based on other experimental results. We note that the interaction between rotating electric fields and trapped non-neutral plasmas involves many complicated processes, and a theoretical prediction is not yet available [10].

- Beam Distribution in Trap before Extraction:
  The equilibrium plasma of cooled antiprotons was generated based on an analytical solution.

- Extraction and Beam Transport:
  The WARP code was used again for the simulations of extraction and transport of the antiprotons in the final equilibrium, starting from the trap region to the position of the positronium target.

2022 JINST 17 T10003

3.1 Injection and trapping

The antiproton beam is decelerated to 100 keV in the ELENA ring, and passed through the pulsed high-voltage decelerator. The antiproton parameters extracted from ELENA [15] are listed in table 1.

Table 1. Beam parameters of antiprotons extracted from the ELENA ring [15].

Parameter	Value
Intensity per Bunch	4.5×10^6
Kinetic Energy	100 [keV]
Momentum Spread ($\Delta p/p$, 95%)	2.5×10^{-3}
Bunch Length (95%)	300 [ns]
Horizontal Emittance (95%)	6 [π mm $\cdot$ mrad]
Vertical Emittance (95%)	4 [π mm $\cdot$ mrad]

In the decelerator, the energy of the antiproton beam is reduced from 100 to 1 keV. The momentum spread and emittance increase 10 times as the energy decreases 100 times, and the beam size is determined by the optics of the decelerator [16] as shown in table 2.

Table 2. Expected beam parameters of antiprotons after the decelerator.

Parameter	Value
Kinetic Energy	1–5 [keV]
Momentum Spread ($\Delta p/p$, 95%)	2.5×10^{-2}
Bunch Length (95%)	300 [ns]
Horizontal Emittance (95%)	60 [π mm $\cdot$ mrad]
Vertical Emittance (95%)	40 [π mm $\cdot$ mrad]
Horizontal Size (95%)	19.7 [mm][16]
Vertical Size (95%)	17.0 [mm][16]

In the simulation, the size and emittance of the antiproton beam injected into the trap were fixed based on table 2. The Twiss parameters [17] α_{Twiss} and β_{Twiss}, which are related to the transverse divergence and size of the beam, and the distance to the trap were set to various values. The purpose of the simulation is to confirm whether the antiproton beam can be injected correctly in the high magnetic field (7 T) region without significant mirroring, and eventually caught in the trap. The trapping efficiencies are plotted in figure 6.

Figure 7 and table 3 show the motions of the injected antiprotons and beam parameters after trapping, respectively, for the case that the initial injection point is 1 m upstream of the trap center and $\alpha_{\mathrm{Twiss}} = 0$ there.

The repetition rate of ELENA is about 110 s [15, 18] and the expected intensity is 4.5×10^6 antiprotons per bunch. Therefore, several bunches are stacked to satisfy the required number of antiprotons at the target. For example, if the trap takes four ELENA cycles, it takes less than 8 min.

2022 JINST 17 T10003

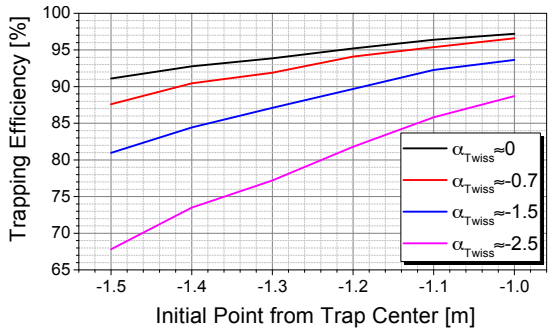

Figure 6. Trapping efficiency as a function of the initial point from the trap center for various α_{Twiss} values.

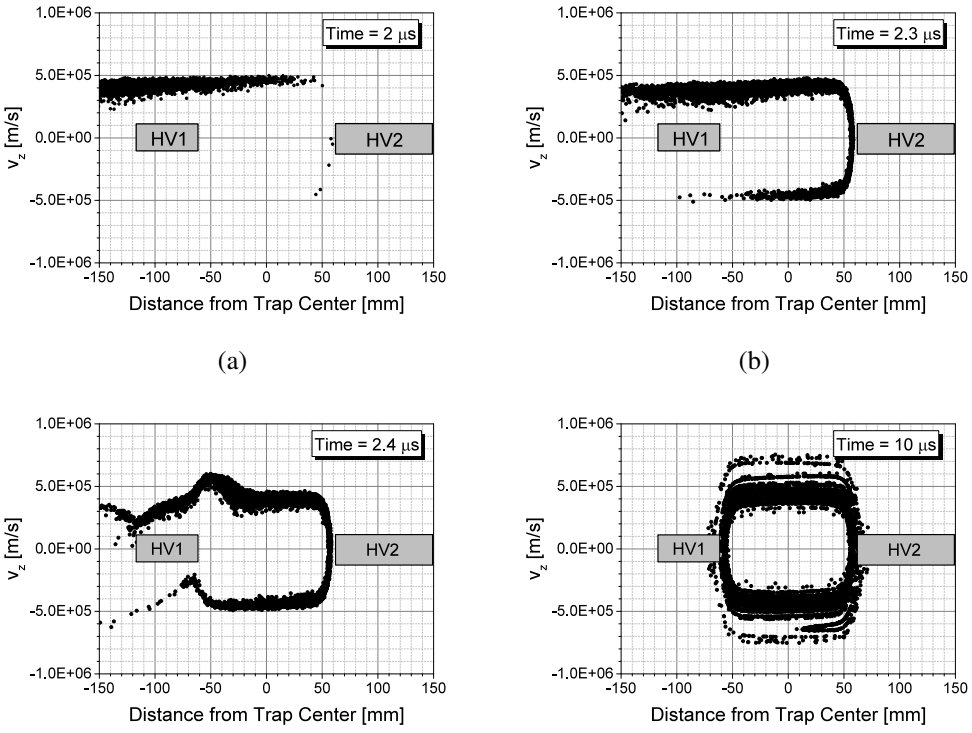

Figure 7. Motions of injected antiprotons in the longitudinal phase-space during trapping. After (a) 2 µs, (b) 2.3 µs (reflected by the downstream HV electrode), (c) 2.4 µs (after turning on the upstream HV electrode) and (d) 10 µs. Here, the initial injection point is 1 m upstream of the trap center, where $\alpha_{\mathrm{Twiss}} = 0$. The number of simulation particles initially used is 10000, and the number of trapped particles in (d) is about 9700.

2022 JINST 17 T10003

Table 3. Beam parameters of trapped antiprotons. Note that here bunch length and beam sizes are given in rms (one standard deviation) values unlike the 95% values used in tables 1 and 2.

Parameter	Value
Kinetic Energy	$\sim$ 950 [eV]
Energy Spread (σ_E, rms)	$\sim$ 450 [eV]
Bunch Length (σ_z, rms)	$\sim$ 37 [mm]
Horizontal Size (σ_x, rms)	$\sim$ 0.50 [mm]
Vertical Size (σ_y, rms)	$\sim$ 0.53 [mm]

3.2 Electron cooling and radial compression

The characteristic cooling time of an electron in a magnetic field owing to cyclotron emission [19] is

$$\tau_c \approx (4\pi\epsilon_0)\frac{3m_e c^3}{4e^2\omega_c^2} \qquad \text{(MKS units)}, \tag{3.1}$$

where m_e, ϵ_0, c, and e are the electron mass, permittivity of free space, speed of light, and elementary charge in the MKS units, respectively, and $\omega_c = eB/m_e$ is the electron cyclotron frequency. For example, τ_c for electrons in a magnetic field of 7 T is $\sim$ 53 ms. For an ideal and optimistic situation, the electron temperature at equilibrium tends to the ambient temperature inside the trap (T_{ambient}), which could decrease to as low as 10 K in the cryogenic system. The antiproton temperature is reduced by energy exchange from collisions with electrons, and its damping rate is given by [19, 20] (assuming that electron bunch and antiproton bunch have the same transverse size)

$$\tau_{\bar{p}} = (4\pi\epsilon_0)^2\,\frac{m_{\bar{p}}m_e}{e^4}\,\frac{1}{n_e \ln\Lambda}\left(\frac{k_B T_{\bar{p}}}{m_{\bar{p}}} + \frac{k_B T_e}{m_e}\right)^{(3/2)}, \tag{3.2}$$

where $\ln\Lambda$ is Coulomb logarithm [21–24] which depends on the density and temperature of the plasmas, and the magnetic field strength.

Equation (3.3) gives the energy loss equation for antiprotons by electrons. The total energy change of electrons including both energy gain from the collisions with antiprotons and loss by the cyclotron emission of electrons is represented by eq. (3.4) [19].

$$\frac{\partial T_{\bar{p}}}{\partial t} = -\frac{1}{\tau_{\bar{p}}}\left(T_{\bar{p}} - T_e\right), \tag{3.3}$$

$$\frac{\partial T_e}{\partial t} = \frac{1}{\tau_{\bar{p}}}\frac{N_{\bar{p}}}{N_e}\left(T_{\bar{p}} - T_e\right) - \frac{2}{3\tau_c}\left(T_e - T_{\text{ambient}}\right). \tag{3.4}$$

Here, τ_c has 3/2 factor because the cyclotron cooling affects the perpendicular electron energy only. The cooling time from 1 keV to 50 eV (95% reduction) of the antiproton is approximately 60 s, as shown in figure 8, when $N_{\bar{p}} = 1\times10^7$, $N_e = 1\times10^8$, $n_{\bar{p}} = 1.0\times10^{13}\,\text{m}^{-3}$, $n_e = 3.9\times10^{13}\,\text{m}^{-3}$. We note that approximately one or two orders of magnitude more electrons are typically used for the antiproton cooling [25]. We emphasize that a simplified and conservative model was adopted here to estimate the scale of the cooling time and to confirm whether it is shorter than the repetition time of the trap operation ($\sim$ 110 s).

2022 JINST 17 T10003

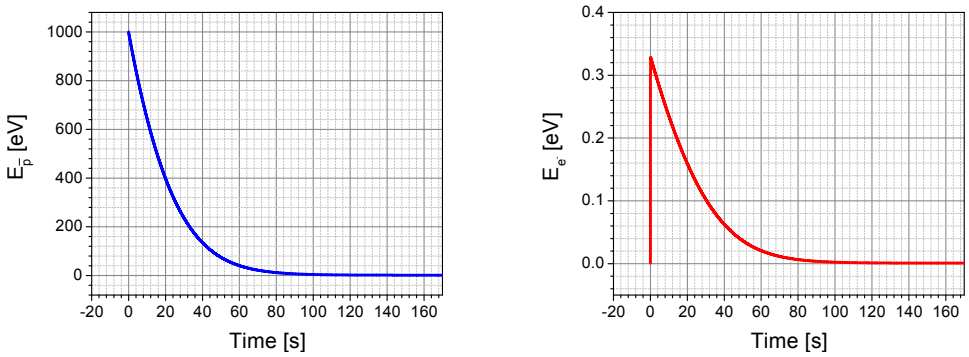

(a) (b)

Figure 8. Changes of (a) antiproton and (b) electron energies.

After electron cooling, electrons are ejected by changing the voltages of HV1, SE1-2 and CE1-3 to zero. From the mass difference between antiprotons and electrons, only electrons are fast removed (within $\sim$ 500 ns), and then voltages of the electrodes are returned to their original values [26]. Our simulation results suggest that the properties of remained antiprotons are nearly unchanged. The remained antiprotons in the potential well are radially compressed by the rotating wall, as shown in figure 9. One electrode of MRE is azimuthally segmented into four pieces, to which RF voltages with different phases are applied. This scheme, known as the rotating-wall technique [12], has been adopted for many antimatter experiments. Surko group [27] applied the technique for the mixture of positrons and electrons, whereas the ALPHA [28] and AE$\bar{g}$IS [26] experiments applied it for the mixture of antiprotons and electrons. The ASACUSA group reported the successful radial compression of a pure antiproton cloud (without electrons) using the rotating-wall technique [29]. For the initial experiment, we plan to attempt the ASACUSA group's approach first. If the compression efficiency turns out to be too low, then we will consider compressing antiprotons together with electrons.

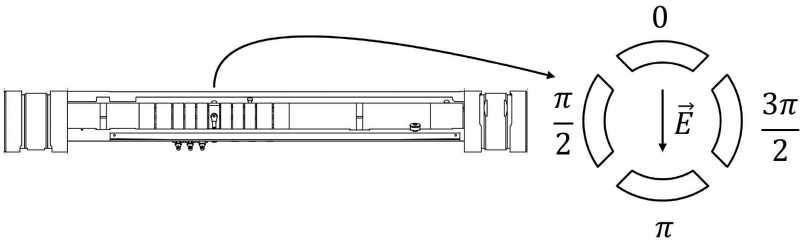

Figure 9. Concept of rotating-wall technique on segmented electrode. This figure shows the case of a dipole drive. The sinusoidal potentials applied to each azimuthal sector ($j = 1, 2, 3, 4$) are $\phi_j = (V_r/2)\cos[2\pi f_r t - \pi/2(j-1)]$, where f_r is the rotating wall frequency (typically, 200–1000 kHz) and V_r is the peak-to-peak amplitude (typically, a few volts).

In previous antiproton experiments [7, 28–30], the outer radius of the compressed antiprotons was reported to be approximately $\sim$ 0.5 mm with a 7 T magnetic field. Hence, for the GBAR trap which is expected to have similar operating conditions, we assume that a 0.5 mm outer radius would be achieved. The duration of the rotating wall t_r is typically around 200 s.

2022 JINST 17 T10003

3.3 Equilibrium of Cooled Antiprotons in Harmonic Potential Well (HPW)

The Penning-Malmberg trap forms an axial potential well with an approximately quadratic form along the axis, called the Harmonic Potential Well (HPW). The distribution of antiprotons in HPW after cooling can be predicted by the equilibrium properties of non-neutral plasma [31, 32]. In the Penning-Malmberg trap, the applied electrostatic potential distribution is approximated by

$$\phi_{\text{apply}}(r,z) = V_0\left(\frac{2z^2 - r^2}{2L^2 + b^2}\right) + \delta, \tag{3.5}$$

where L (= 0.04 m) is the distance from the trap center to the center of the SE3 electrode, and b (= 0.015 m) is the inner radius of the trap electrodes. Here, δ is the offset and V_0 is the trap potential depth, which is a negative value for antiproton trapping. The axial motion of the trapped antiprotons in HPW is a harmonic oscillation with an axial oscillation frequency of ω_z, which is determined by L and b, and the potential distribution on the axis [32]:

$$\phi_{\text{apply}}(0,z) = -\frac{1}{2}\frac{m_{\bar{p}}}{e}\omega_z^2 z^2 + \delta, \tag{3.6}$$

$$\omega_z^2 = \frac{4e|V_0|}{m_{\bar{p}}\left(2L^2 + b^2\right)}. \tag{3.7}$$

In the GBAR trap, the MRE configuration is used to compensate for the self-potential produced by the plasma [11]. By setting appropriate voltages on each small electrode, a potential well of more precise quadratic shape can be generated. The potential map in the antiproton trap can be obtained by analytic calculation or numerical simulation, as shown in figure 10.

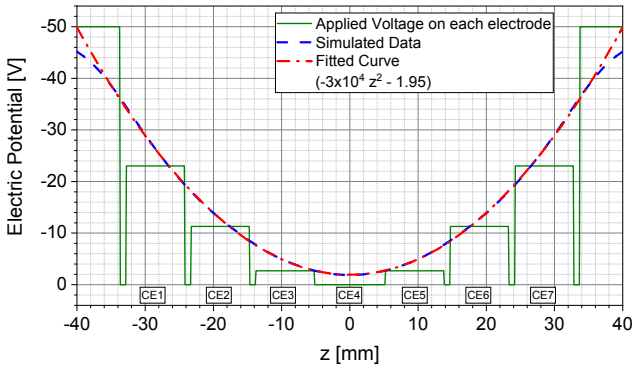

Figure 10. Electrostatic potential distribution of HPW along the trap axis.

The simulated potential map can be used to estimate the axial oscillation frequency ω_z. The fitting equation for the simulated potential distribution shown in figure 10 in the quadratic form is $\phi_{\text{sim}}(0,z) = -3\times10^4 z^2 - 1.95$. Compared with eq. (3.6), the axial oscillation frequency is obtained as

$$\omega_z = \sqrt{3\times10^4\frac{2e}{m_{\bar{p}}}}, \tag{3.8}$$

2022 JINST 17 T10003

which is used in the calculation for the equilibrium. The characteristics of the non-neutral plasmas were used to calculate the cooled antiprotons in equilibrium. In HPW, the non-neutral plasmas in equilibrium have a spheroidal shape determined by the plasma density and the potential distribution [32]. Therefore, the shape of the cold (in the limit of zero temperature) antiprotons in HPW can be obtained analytically. When non-neutral plasmas reach equilibrium, the axial space-charge potential generated by the plasmas cancels the applied potential. Parameters $\alpha_{\rm eq}$ and $\beta_{\rm eq}$ represented in eqs. (3.9), (3.10), and (3.11) give the size of non-neutral plasmas satisfying the above condition. It should be noted that $\alpha_{\rm eq}$ and $\beta_{\rm eq}$ in eqs. (3.9) are related to the plasma density and the applied potential as

$$\alpha_{\rm eq} = 1 - \frac{\omega_z^2}{\omega_p^2}, \qquad \beta_{\rm eq} = \frac{2\omega_z^2}{\omega_p^2}, \qquad \omega_p^2 = \frac{ne^2}{\epsilon_0 m}, \tag{3.9}$$

where ω_p is the plasma frequency, n is the plasma density and ϵ_0 is the vacuum permittivity.

Equations (3.10) and (3.11) show the relationship between the parameters and the plasma sizes for oblate ($z_b < r_b$) and prolate ($z_b > r_b$) spheroids (see section 4.3.1 of ref. [32] for details).

$$\begin{cases} \alpha_{\rm eq} = -\dfrac{1}{\frac{r_b^2}{z_b^2}-1} + \dfrac{\frac{r_b^2}{z_b^2}}{\left(\frac{r_b^2}{z_b^2}-1\right)^{3/2}} \tan^{-1}\left(\dfrac{r_b^2}{z_b^2}-1\right)^{1/2} \\ \dfrac{1}{2}\beta_{\rm eq} = \dfrac{\frac{r_b^2}{z_b^2}}{\frac{r_b^2}{z_b^2}-1} - \dfrac{\frac{r_b^2}{z_b^2}}{\left(\frac{r_b^2}{z_b^2}-1\right)^{3/2}} \tan^{-1}\left(\dfrac{r_b^2}{z_b^2}-1\right)^{1/2} \end{cases} \qquad (z_b < r_b), \tag{3.10}$$

$$\begin{cases} \alpha_{\rm eq} = \dfrac{1}{1-\frac{r_b^2}{z_b^2}} - \dfrac{\frac{r_b^2}{z_b^2}}{2\left(1-\frac{r_b^2}{z_b^2}\right)^{3/2}} \ln\left[\dfrac{1+\left(1-\frac{r_b^2}{z_b^2}\right)^{1/2}}{1-\left(1-\frac{r_b^2}{z_b^2}\right)^{1/2}}\right] \\ \dfrac{1}{2}\beta_{\rm eq} = -\dfrac{\frac{r_b^2}{z_b^2}}{1-\frac{r_b^2}{z_b^2}} + \dfrac{\frac{r_b^2}{z_b^2}}{2\left(1-\frac{r_b^2}{z_b^2}\right)^{3/2}} \ln\left[\dfrac{1+\left(1-\frac{r_b^2}{z_b^2}\right)^{1/2}}{1-\left(1-\frac{r_b^2}{z_b^2}\right)^{1/2}}\right] \end{cases} \qquad (z_b > r_b), \tag{3.11}$$

where r_b and z_b are the radial and axial dimensions, respectively.

The relationship between r_b and z_b is calculated using the above equations and is plotted in figure 11. The density is given by $n = N/\left[\frac{4}{3}\pi r_b^2 z_b\right]$ and N is the total number of antiprotons in the trap. This calculation assumed that $N = 1 \times 10^7$, which is typically required in the experiment.

3.4 Extraction and beam transport

As discussed in section 3.2 the trapped antiprotons are compressed by the rotating-wall technique, and it is assumed that the plasma outer radius (r_b) becomes about 0.5 mm and the plasma half-length (z_b) is approximately 13 mm as shown in figure 11. For 1×10^7 antiprotons, the initial beam distribution data before extraction can be generated by using these dimensions as shown in figure 12.

Before the beam was extracted in the simulation, the HPW was moved downstream by changing the voltages applied to the MRE, as illustrated in figure 13(a) to prevent the beam size from increasing.

2022 JINST 17 T10003

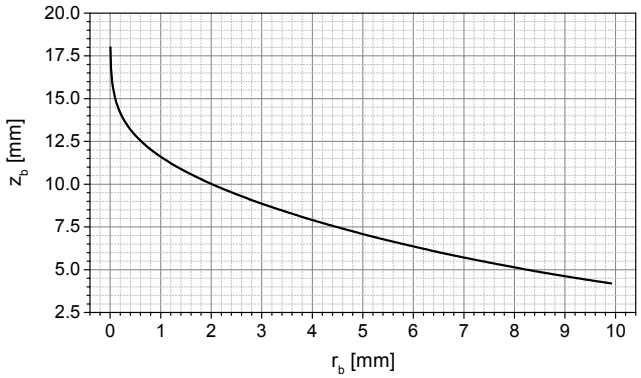

Figure 11. Relation between r_b and z_b when 1×10^7 antiprotons are in the harmonic potential well represented in figure 10.

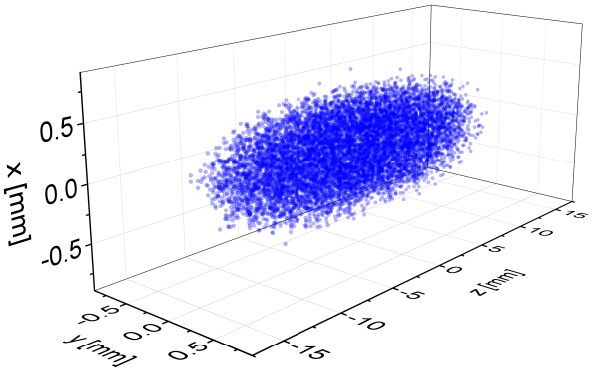

Figure 12. Initial antiproton distribution before extraction. The number of antiprotons is 1×10^7 and their energy is assumed ~ 0 K in the cold plasma limit.

The shape of the HPW was kept the same during this process, and the antiprotons were moved 19 mm downstream maintaining their distribution. The antiproton beam was pushed by the slope of the electric potential, made as shown in figure 13(b), and the mean energy was approximately 100 eV.

The downstream HV electrode (HV2) of the MRE, which is the longest (110 mm in length) electrode in figure 2, was used for acceleration and bunch compression. The production cross sections of antihydrogen ions are maximum when the impact energy of the antiproton is approximately 6 keV for the ground state Ps, and < 1 keV for the excited Ps [33, 34]. Therefore, the beam energy was raised to 6 keV using the HV2 electrode by applying a pulsed high voltage.

$\bar{\mathrm{H}}$ productivity increases when the bunch length (in time) of the antiproton is shorter than the lifetime of the Ps target which is 142 ns [35]. A double-gap buncher (DGB) system [36, 37] is employed to compress the beam length. The DGB system pulls particles to the beam center by applying the RF or sawtooth-shaped voltage across the two gaps between the center electrode and ground electrodes at both sides.

With the combination of above two systems as shown in figure 14(a), the required values of the energy and bunch length of the extracted antiprotons can be obtained. The HV2 electrode

2022 JINST 17 T10003

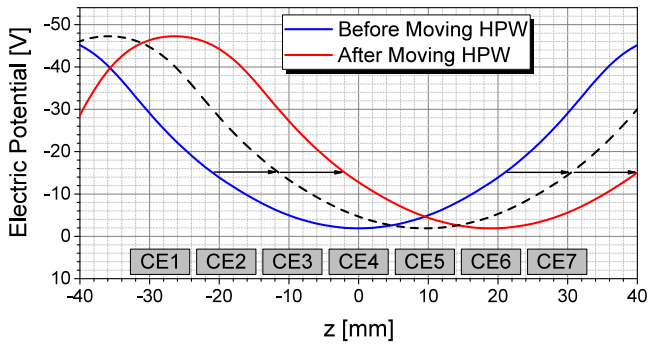

(a)

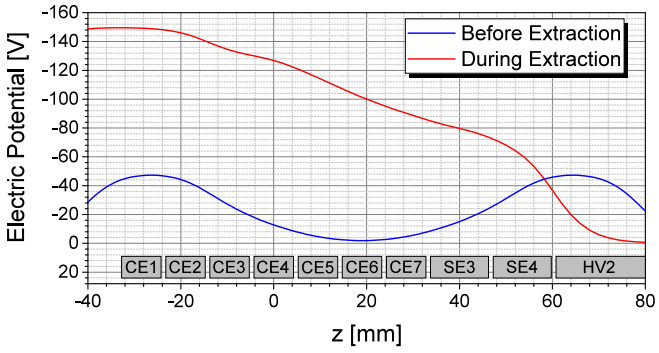

(b)

Figure 13. On-axis potential distributions for (a) moving HPW and (b) extracting antiprotons.

plays the role of the center electrode in figure 14(a). The extracted beam into the HV2 is in the 1st bunching process, and the HV2 is pulsed to −6 kV when the beam goes through the HV2. Finally, the beam coming out from the HV2 experiences the 2nd bunching process. With these processes, the extracted beam is accelerated to 6 keV and its length is compressed. Here, we use a voltage waveform composed of a sawtooth-shaped voltage and pulsed high voltage [see figure 14(b)] on the downstream HV electrode during the extraction.

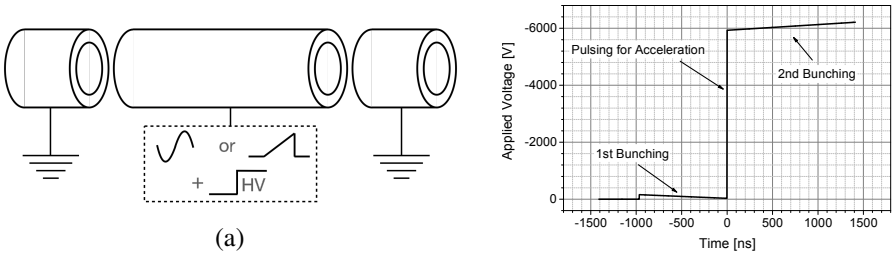

(a) (b)

Figure 14. (a) Concept of simultaneous acceleration and bunch compression. (b) Voltage waveform applied to the downstream HV electrode.

2022 JINST 17 T10003

After extraction, two einzel lenses and an EQT were used to transport the antiproton beam and focus its size on the target. In the simulation with the WARP code, the voltages applied to each component were −2500 V, −2200 V, and ±170 V.

At the target position, the antiprotons have energy and time distributions, as shown in figure 15, respectively, and their mean energy, energy spread, and bunch length are $\bar{E} = 6.01$ keV, $\sigma_E = 11.57$ eV, and $\sigma_t = 56.17$ ns, respectively.

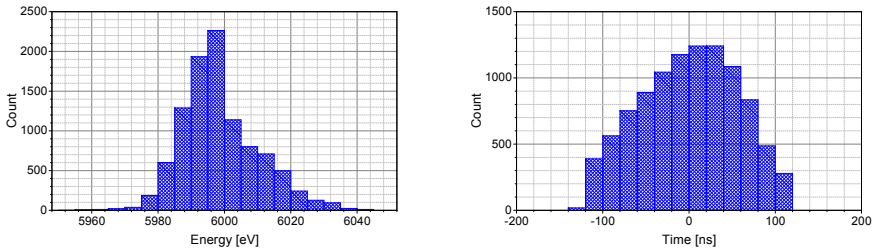

(a) (b)

Figure 15. (a) Energy and (b) time distributions of antiprotons at Ps target.

Another critical parameter is the transverse beam size, which should be within the target size. The Ps target cavity has a 2 mm × 2 mm cross section and is planned to be further reduced to 1 mm × 1 mm [4]. For the simulation results in figure 16, the transverse size is $\sigma_x = 0.677$ mm horizontally and $\sigma_y = 0.512$ mm vertically.

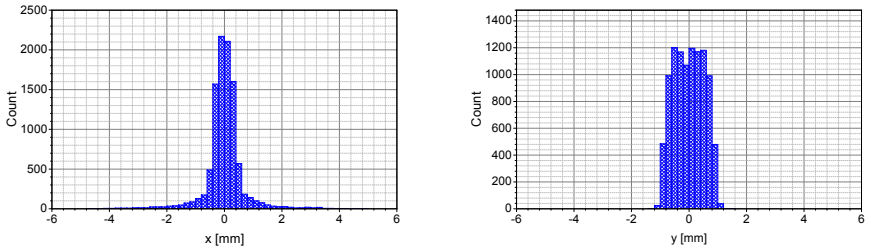

(a) (b)

Figure 16. (a) Horizontal and (b) vertical distributions of antiprotons at Ps target.

In particular, 90.7% of the antiprotons remains within the target hole of 2 mm × 2 mm [the white box in figure 17(a)] and 45.0% within 1 mm × 1 mm. The phase-space plots in figures 17(b) and 17(c) show that the focal plane of the beam is matched to the target position with the transverse emittances of $\epsilon_x = 2.83$ mm · mrad and $\epsilon_y = 1.92$ mm · mrad, respectively.

4 Summary

We have presented the design concept and simulation results of the GBAR antiproton trap, which will be used to accumulate the antiproton beams and manipulate them for maximum interactions with the GBAR positronium target. We confirmed from the simulations that approximately 1×10^7

2022 JINST 17 T10003

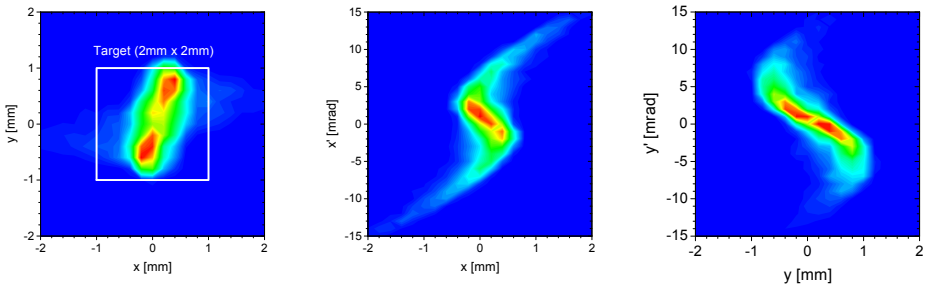

(a) (b) (c)

Figure 17. (a) Transverse distribution, (b) horizontal, and (c) vertical phase spaces of antiprotons at Ps target.

antiprotons can be confined in the trap and extracted with 6 keV of energy. We anticipate ~ 90% of the accumulated antiprotons would be transported to the target of 2 mm × 2 mm in size. While well-established technologies were adopted, we carefully optimized each trap component based on theoretical estimations and 3D PIC simulations. Fabrications of MRE and UHV bore were finished, and the SC magnets and vacuum system were tested. Control and high-voltage systems are currently under development. We will test the loading of the electron beam first, and subsequently try injection and trapping of the antiprotons. Depending on the test results, it might be necessary to modify the electrode system to suit various experimental conditions.

Acknowledgments

This work was supported by the Ministry of Education of the Republic of Korea and the National Research Foundation of Korea (NRF-2016R1A6A3A11932936, NRF-2021R1A2C3010989, NRF-2016R1A5A1013277).

References

[1] GBAR collaboration, *Proposal to measure the gravitational behaviour of antihydrogen at rest*, Tech. Rep., SPSC-P-342, CERN, Geneva, Switzerland (2011).

[2] P. Perez, D. Banerjee, F. Biraben, D. Brook-Roberge, M. Charlton, P. Cladé et al., *The GBAR antimatter gravity experiment*, *Hyperfine Interact.* **233** (2015) 21.

[3] L. Hilico, J.-P. Karr, A. Douillet, P. Indelicato, S. Wolf and F.S. Kaler, *Preparing single ultra-cold antihydrogen atoms for free-fall in GBAR*, *Int. J. Mod. Phys. Conf. Ser.* **30** (2014) 1460269 [arXiv:1402.1695].

[4] B.M. Latacz, *Study of the antihydrogen atom and ion production via charge exchange reaction on positronium*, Ph.D. thesis, Université Paris-Saclay, Paris, France (2019).

[5] P. Comini, P.-A. Hervieux and F. Biraben, $\bar{H}^+$ *production from collisions between positronium and keV antiprotons for GBAR*, *Hyperfine Interact.* **228** (2014) 159.

[6] A. Husson et al., *A pulsed high-voltage decelerator system to deliver low-energy antiprotons*, *Nucl. Instrum. Meth. A* **1002** (2021) 165245.

2022 JINST 17 T10003

[7] N. Kuroda et al., *Development of a monoenergetic ultraslow antiproton beam source for high-precision investigation*, *Phys. Rev. ST Accel. Beams* **15** (2012) 024702.

[8] G. Zwicknagel, *Electron cooling of ions and antiprotons in traps*, *AIP Conf. Proc.* **821** (2006) 513.

[9] ATRAP collaboration, *Stacking of cold antiprotons*, *Phys. Lett. B* **548** (2002) 140.

[10] J. Fajans and C.M. Surko, *Plasma and trap-based techniques for science with antimatter*, *Phys. Plasmas* **27** (2020) 030601.

[11] T. Mohamed, A. Mohri and Y. Yamazaki, *Comparison of non-neutral electron plasma confinement in harmonic and rectangular potentials in a very dense regime*, *Phys. Plasmas* **20** (2013) 012502.

[12] F. Anderegg, *Rotating wall technique and centrifugal separation*, in *Trapped Charged Particles: A Graduate Textbook with Problems and Solutions*, pp. 221–238, World Scientific (2016).

[13] A. Friedman, D.P. Grote and I. Haber, *Three-dimensional particle simulation of heavy-ion fusion beam*, *Phys. Fluids* **4** (1992) 2203.

[14] G. Bettega, F. Cavaliere, M. Cavenago, A. Illiberi, R. Pozzoli and M. Romé, *Experimental and numerical analysis of the electron injection in a malmberg-penning trap*, *Phys. Plasmas* **14** (2007) 042104.

[15] W. Bartmann, P. Belochitskii, H. Breuker, F. Butin, C. Carli, T. Eriksson et al., *The ELENA facility*, *Phil. Trans. Roy. Soc. A* **376** (2018) 20170266.

[16] A. Husson, *Deceleration of antiprotons from CERN's ELENA synchrotron and transport of antimatter beams through the GBAR experiment*, Ph.D. thesis, Université Paris Saclay, Paris, France (2018).

[17] M. Reiser, *Theory and design of charged particle beams*, John Wiley & Sons (2008).

[18] M. Charlton et al., *Positron production using a 9 MeV electron linac for the GBAR experiment*, *Nucl. Instrum. Meth. A* **985** (2021) 164657 [arXiv:2006.05966].

[19] M. Vogel, *Particle Confinement in Penning Traps*, Springer (2018).

[20] T.M. O'Neil, *Cooling of a pure electron plasma by cyclotron radiation*, *Phys. Fluids* **23** (1980) 725.

[21] D. Sivukhin, *Coulomb collisions in a fully ionized plasma*, *Rev. Plasma Phys.* **4** (1966) 93.

[22] J.A. Krommes, *An introduction to the physics of the coulomb logarithm, with emphasis on quantum-mechanical effects*, *J. Plasma Phys.* **85** (2019) 925850101.

[23] D. Montgomery, *Magnetic field dependence of plasma relaxation times*, *Phys. Fluids* **17** (1974) 2201.

[24] C. Toepffer, *Scattering of magnetized electrons by ions*, *Phys. Rev. A* **66** (2002) 022714.

[25] G. Gabrielse, X. Fei, L.A. Orozco, R.L. Tjoelker, J. Haas, H. Kalinowsky et al., *Cooling and Slowing of Trapped Anti-protons Below 100-MeV*, *Phys. Rev. Lett.* **63** (1989) 1360.

[26] S. Aghion et al., *Compression of a mixed antiproton and electron non-neutral plasma to high densities*, *Eur. Phys. J. D* **72** (2018) 76 [*Erratum ibid.* **73** (2019) 234]

[27] J.R. Danielson and C.M. Surko, *Torque-balanced high-density steady states of single-component plasmas*, *Phys. Rev. Lett.* **94** (2005) 035001.

[28] ALPHA collaboration, *Compression of Antiproton Clouds for Antihydrogen Trapping*, *Phys. Rev. Lett.* **100** (2008) 203401 [arXiv:0806.4791].

[29] N. Kuroda et al., *Radial Compression of an Antiproton Cloud for Production of Intense Antiproton Beams*, *Phys. Rev. Lett.* **100** (2008) 203402.

2022 JINST 17 T10003

[30] A. Gutierrez, M. Ashkezari, M. Baquero-Ruiz et al., *Antiproton cloud compression in the ALPHA apparatus at CERN*, *Hyperfine Interact.* **235** (2015) 21.

[31] D.H.E. Dubin and T.M. O'Neil, *Trapped nonneutral plasmas, liquids, and crystals (the thermal equilibrium states)*, *Rev. Mod. Phys.* **71** (1999) 87.

[32] R.C. Davidson, *Physics of Nonneutral Plasmas*, Imperial College Press (London) (2001).

[33] P. Comini and P.A. Hervieux, *$\bar{H}$ and $\bar{H}^+$ production cross sections for the GBAR experiment*, *J. Phys. Conf. Ser.* **443** (2013) 012007.

[34] P. Comini and P.A. Hervieux, *$\bar{H}^+$ ion production from collisions between antiprotons and excited positronium: cross sections calculations in the framework of the GBAR experiment*, *New J. Phys.* **15** (2013) 095022 [*Erratum ibid.* **23** (2021) 029501]

[35] B.H. Kim et al., *Development of a $PbWO_4$ Detector for Single-Shot Positron Annihilation Lifetime Spectroscopy at the GBAR Experiment*, *Acta Phys. Polon. A* **137** (2020) 122.

[36] G.D. Kim, W. Hong, H.J. Woo, J.K. Kim, C.H. Eum, J.H. Chang et al., *Design of a nanosecond beam bunching system*, *J. Radioanal. Nucl. Chem.* **271** (2007) 547.

[37] J.H. Kim and Y.S. Kim, *Simulation study of a double-gap particle buncher for low-energy protons*, *J. Korean Phys. Soc.* **61** (2012) 189.

2022 JINST 17 T10003